The corrosion inhibition mechanisms of Ce(III) ions and triethanolamine on graphite—AA2024-T3 galvanic couples revealed by localised electrochemical techniques

L.B. Coelho[a,*], M. Taryba[b], M. Alves[b], X. Noirfalise[c], M.F. Montemor[b], M.-G. Olivier[a,c]

[a] Materials Science Department, Faculty of Engineering, University of Mons, 20 Place du Parc, 7000 Mons, Belgium
[b] Centro de Quimica Estrutural, Instituto Superior Técnico, Universidade de Lisboa, Av. Rovisco Pais, 1049-001 Lisboa, Portugal
[c] Materia Nova asbl, Avenue Copernic 1, 7000 Mons, Belgium

ABSTRACT

The inhibition mechanism of cerium chloride and triethanolamine on the galvanic corrosion of AA2024-T3/graphite in NaCl electrolyte was investigated by localised electrochemical techniques. Quasi-simultaneous measurements of ionic current densities and pH were performed by the Scanning Vibrating Electrode Technique (SVET) and Scanning Ion-Selective Electrode Technique (SIET). Surfaces were analysed by Scanning Electron Microscopy coupled with Energy Dispersive X-ray (SEM-EDX) and X-Ray Photoelectron Spectroscopy (XPS). This work follows a recent publication (Coelho et al. 2018) and discusses the effect of inhibitors on two AA2024-T3/graphite galvanic couples, constructed with two different areas ratio, evidencing that this parameter significantly influences the corrosion and corrosion inhibition process.

1. Introduction

Aluminium alloys are susceptible to intense corrosion processes when galvanically coupled with Carbon Fibre-Reinforced Polymers (CFRP) [1–5]. In aeronautical junctions, this issue is minimized by applying insulating coatings between CFRP and the aluminium alloys plates. For instance, G-10 fiberglass is used to avoid direct contact between the parts, thus working as an electronic/ionic barrier [2,6]. Nonetheless, in case of local failure, an electrical circuit might be created between the two dissimilar materials: the alloy and CFRP. Thereby, the presence of moisture and aggressive species (e.g. chloride ions) leads to formation of a persistent Cl⁻-containing electrolyte layer, over both materials [5]. As consequence, corrosion of the aluminium alloy can be significantly accelerated, while the carbon-fibres, playing the role of cathode, remain protected.

Various coating systems, free of hazardous Cr(VI), have been recently discussed for corrosion protection of aluminium alloys [7–15]. Concerning the particular case of AA2024, different inhibitor systems have been proposed to offer corrosion protection, either as electrochemically active species or barriers layers [16–19]. In a preliminary work [20], AA2024-T3/graphite galvanic couples were exposed to 12.00 mM NaCl electrolytes and the inhibition efficiency of several compounds was studied by the SVET and ZRA (Zero Resistance

Ammeter) techniques. The results suggest that some inhibitors offer efficient corrosion protection and amongst these, cerium chloride and triethanolamine, appear to be promising candidates for reducing galvanic corrosion effects. Cerium salts, and in particular Ce (III) – containing species, have been successfully applied as corrosion inhibitors for protecting aluminium alloys for more than 30 years [21–24]. In near-neutral solutions, these salts are known to inhibit the oxygen reduction reaction (ORR) by forming protective corrosion products that restrict the diffusion of dissolved oxygen to the cathodic sites.

Triethanolamine (TEA) is a commercially available, environment-friendly and versatile compound that forms coordination compounds with different metals [25]. Triethanolamine has recently been used as corrosion inhibitor and it was shown that it blocks active corrosion sites by absorbing on the metal surface. Studies carried out on steel [26] and Mg alloys [27] propose that TEA assists metal passivation, even if corrosion activity is already ongoing. The good solubility of TEA in water has been considered as one reason for poorer protection at longer term [26]. Although several studies [26,28] refer to physical adsorption based-mechanisms, only few [27,29] report that TEA chemically interacts with the surface due to coordination of the heteroatoms with metallic impurities. For instance, Dumitriu et al. [30] reports that TEA behaves like N- and O-donor ligands with diverse coordination modes. In fact, recent work has shown that TEA can assist electrodeposition of

---

Cu and Zn by complexing both Cu^{2+} and Zn^{2+} ions [25].

Conventional electrochemical techniques, such as polarisation curves, electrochemical impedance spectroscopy and ZRA, lack spatial resolution, offering averaged information from the working electrode. Local electrochemical techniques provide details of the corrosion process with microscopic resolution. On the one hand, SVET can identify anodic and cathodic spots as well as the current densities and their evolution in time; on the other hand, SIET works as tool for pH (or other ionic specie) monitoring [31,32]. The complementary information obtained from these two techniques (electrochemical oxidation-reduction processes via SVET and acid-base chemical equilibria via SIET) are of prime importance to understand the corrosion processes, particularly localized ones. Measurements can be made sequentially [33] or, as proposed elsewhere, quasi-simultaneously [34]; this approach makes SVET and SIET powerful tools to explain the electrochemical/chemical reactions governing corrosion and corrosion inhibition mechanisms in various systems [35–41].

In a recent study [1] the authors studied the effect of the area of the electrodes in the galvanic couple AA2024-T3/graphite and discussed its role on the corrosion mechanism. The study employed several techniques, including SVET/SIET and SEM-EDX. It was shown that AA2024, in the couple with the highest AA2024 to graphite area ratio (10), presented both anodic and cathodic activities, which resulted in trenching of the matrix around cathodic precipitates. Concerning the couple with the lowest area ratio (1.5), more generalised anodic dissolution of AA2024 was noticed, including corrosion of the matrix and grain boundaries (intergranular corrosion). In this sequence, the present work investigated the potential of cerium chloride and TEA as corrosion inhibitors for galvanic couples AA2024-T3/graphite (M1 and M2) with different area ratio. The study explored the combined use of SVET/SIET complemented with SEM-EDX and XPS analysis.

2. Materials and methods

2.1. AA2024/graphite galvanic coupling models

Two AA2024/graphite galvanic couple models, with different area ratio were designed to simulate the galvanic corrosion processes occurring at AA2024/CFRP interfaces. The ratios between the area of AA2024 and that of graphite were 10 and 1.5, respectively designated as M1 and M2 [1]. The AA2024-T3 composition (Q-Lab) was 4.65% Cu, 1.87% Mg, 0.61% Mn, 0.19% Fe, 0.13% Zn, balance Al, while the graphite foil was 99.8% pure (Alfa Aesar). AA2024-T3 plates (1 mm thickness) were cut into ~2 mm coupons. One set of coupons was kept, while another set was abraded using drill tools (Dremel) to form ~0.85 mm diameter rods. Next, the AA2024 specimens were cleaned by acetone/ethanol employing an ultrasonic bath. The alloy and graphite specimens were mounted together and their cross-sections were exposed by grinding with SiC paper (up to the 4000 grade) prior to SVET/SIET measurements. Electrical connections were introduced in the bottom of the specimens, using conductive silver glue and graphite conductive adhesive.

2.2. SVET/SIET measurements

The SVET/SIET system and respective operating parameters were reproduced as previously described [1]. SVET/SIET monitoring was performed quasi-simultaneously [34]. The apparatus and corresponding software were supplied by Applicable Electronics™ and Science Wares™, respectively.

SVET microelectrodes were prepared by deposition of a platinum black on the tips of insulated Pt-Ir probes (MicroProbes™). The probe was vibrated in two perpendicular planes, vertical (Z) and horizontal (X), at frequencies of 124 Hz (Z) and 325 Hz (X), respectively. The probe diameter was 16 μm, the amplitude of vibration was 32 μm (peak to peak) and it was positioned 100 ± 3 μm above the sample surface.

Only the data obtained in the vertical plane of vibration (Z) were considered for analysis. Localised pH measurements were performed using glass-capillary ISMEs. The silanized capillaries were back-filled with an inner reference solution and tip-filled with a selective iono-phore based oil-like membrane [42]. A homemade reference mini-electrode, employing Ag/AgCl wire as inner reference, was used.

The measurements were carried out in 8.25 mM NaCl + 1.25 mM $CeCl_3$ or in 12.00 mM NaCl + 500 ppm (0.5 g/L or 3.35 mM) triethanolamine. pH of the corresponding bulk solutions was ~5.3 and ~7.3, respectively. The total chloride concentration of both solutions was the same of the reference electrolyte (12.00 mM NaCl) considered in the previous work [1]. $CeCl_3 \cdot 7H_2O$ was purchased from Fluka Chemika (≥99.9%) and triethanolamine from Alfa Aesar (≥98.5%). All measurements were performed at room temperature, at least in duplicate, and reproducible results were obtained. The volume of the cell was kept constant, being 7 ml. Small drops of Millipore water were added to the cell during the experiments to keep the volume as fixed and, thus, preventing the interference of the evaporation on the recorded results.

2.3. SEM-EDX analysis

Scanning Electron Microscopy coupled with Energy Dispersive X-ray (SEM-EDX) Spectroscopy experiments were carried out either with a Hitachi S2400 (accelerating voltage of 20 keV) or a JEOL 7001 F FEG-SEM/EDX (accelerating voltage of 15 keV). Reproducibility of the micrographs and elemental compositions was considered.

2.4. X-Ray photoelectron spectroscopy (XPS) analysis

The XPS analysis was performed on a Phi Versa Probe 5000 system (resolution 0.1 eV) using an Al Kα (1486.6 eV) radiation as the excitation source. The spectra were recorded in constant analyser transmission mode and an estimated error of 0.1 eV was assumed for all measurements. The measurements were carried out employing an Al X-Ray source with spot size of 200 μm (50 W) for AA2024 and 20 μm (4.5 W) for graphite. Quantitative analysis was accomplished by determining the elemental peak areas, following a Shirley background subtraction [43]. XPS survey spectra were recorded using 187.85 eV pass energy and the high resolution spectra were taken in the region of interest (Ce 3d photoionization) using 23.35 eV pass energy with a 0.2 eV step. All spectra were corrected for the transmission function of the spectrometer.

3. Results and discussion

3.1. Inhibitive action of cerium on M1

Fig. 1 shows that anodic activity over AA2024 and cathodic activity on graphite decreased over the immersion time. The anodic activity decreased nearly 3 times from 1 h to 20 h and the most intense decrease was noticed at early stages. After approximately 5 h (maps not presented), the magnitude of the anodic and cathodic current densities remained stable up to 20 h. Compared to the results obtained in the absence of inhibitor [1], electrochemical activity was significantly reduced. For instance, after 1 h in the cerium-containing solution, the current densities corresponding to the maximum anodic and cathodic peaks were around 34 and $-18 \mu A/cm^2$, respectively – Fig. 1; while after the same time, in the couple exposed to an inhibitor-free solution, the same peaks reached 320 and $-200 \mu A/cm^2$, respectively. The results indicated a decrease of approximately one order of magnitude of the corrosion activity in the presence of inhibitor, probably due to the precipitation of cerium-based compounds that occurred preferentially over graphite. Ce cations are likely to react with generated OH^-, leading to the formation of protective species. It is worth to stress that no gas release was noticed at the graphite surface, indicating that ORR, and not water reduction, was governing the cathodic process. The
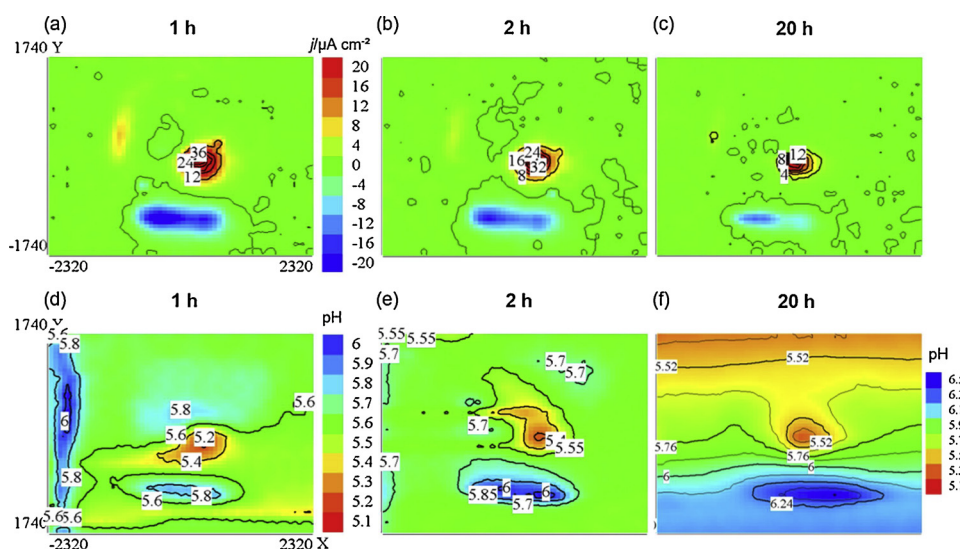
Fig. 1. (a, b, c) Current density (j / μA cm^{-2}) and (d, e) pH maps obtained for the M1 sample exposed to 8.25 mM NaCl + 1.25 mM CeCl$_3$ after: (a, d) 1 h, (b, e) 2 h and (c, f) 20 h. The current density scales are valid for all maps. The pH scale of (d) if valid for (e). X and Y coordinates represent the width of the scan in μm.
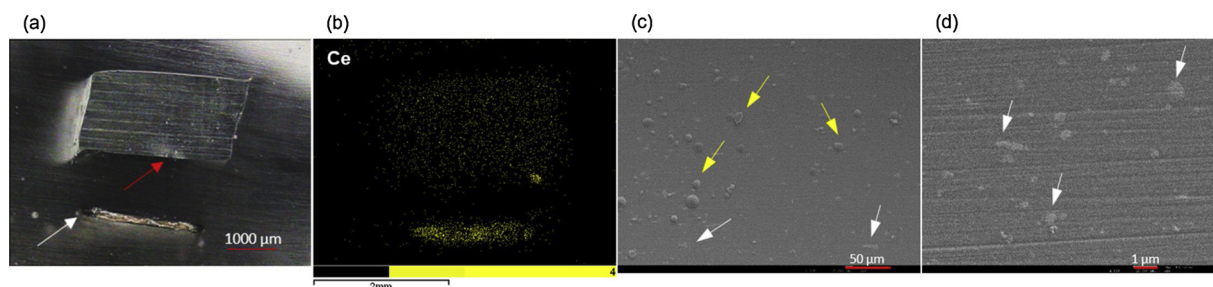

Fig. 2. (a) Optical micrograph of the M1 surface taken in situ during SVET-SIET measurements after 20 h. (b) EDX elemental map of Ce taken from the M1 surface after 20 h of exposure to the 8.25 mM NaCl + 1.25 mM CeCl$_3$ solution. (c, d) SEM images of the AA2024 areas that displayed local alkalinisation at early stages (Fig. 1(d)). The yellow and white arrows indicate intermetallic particles covered and not covered by Ce-based precipitates, respectively (For interpretation of the references to colour in this figure legend, the reader is referred to the web version of this article).

results also demonstrated that the inhibitive effect over the M1 galvanic couple occurred in greater extent at early immersion stages. Nonetheless, one anodic spot remained active throughout the entire test, as indicated by the red arrow in the image taken after 20 h (Fig. 2(a)). The white arrow in the same optical image indicates the graphite region, which was not entirely covered by the Ce-containing precipitates, where the main cathodic activity was located at the end of the test (Fig. 1(c)).

The same conclusions could be drawn by comparing the SIET results obtained in the presence and absence of cerium (III) chloride: the maximum pH values over graphite after 1 h immersion were 5.8 and 9.1 (Fig. 1(d)), respectively in the presence and absence of cerium ions. Concerning the anodic regions on AA2024, although the pH attained similar values (~5.2 after 1 h) in the presence and absence of cerium ions, the acidified areas were much larger in the reference electrolyte (not-inhibited). Therefore, it can be claimed that the inhibition activity induced a marked decrease of the alkaline pH (in cathodic areas) on graphite compared to the acidification gradients on the alloy. This might be related to the fact that OH$^-$ ions produced over graphite are readily consumed by the Ce^{3+} cations, forming precipitates that block the cathodic sites. Conversely, in the anodic zones, concurrent acid-base reactions should not have been affected by the precipitation of Ce hydroxides, yielding pH values that were less affected by precipitation of corrosion products. The SIET map obtained after 20 h (Fig. 1(f)) showed that the acidification process in the anodic zones of the alloy remained controlled, while slight alkalinization around graphite occurred. This trend suggested that Ce^{3+} ions reduced the cathodic activity but could not fully suppress it.

Contrary to the results obtained in the absence of inhibitor, where

cathodic activity was observed on the AA2024 even after 5 h [1], in the presence of cerium ions, cathodic currents could not be measured above the alloy surface. On the one hand, this might be explained by the formation of cerium precipitates over the cathodic intermetallic particles (IMPs) existing on AA2024 that inhibited the development of micro-galvanic couples on the alloy surface. On the other hand, oxygen reduction reaction over graphite continued over time, possibly due to the larger cathodic area and higher nobility compared to the Cu-rich precipitates on AA2024.

It is worth to mention that SIET maps suggested localised weak alkalinisation processes over AA2024, particularly during the first 2 h (Fig. 1(d, e)). Such regions were located between the spots presenting the most intense anodic activity observed in the SVET maps. This slight pH increase might be related to electrochemical reduction of oxygen at the cathodic intermetallics. SIET monitoring allows higher sensitivity compared to SVET (the SIET probe has a smaller tip size and was placed closer to the sample surface) and may detect pH changes, e.g. due to ORR. In all cases, ORR related cathodic activity over IMPs was considerably inhibited by the precipitation of cerium hydroxides, as the alkalinisation was more controlled at early stages of immersion. At the end of the experiments, intermetallics seemed to be protected, without noticeable signs of trenching or de-alloying (see SEM analysis in Fig. 2(c, d)). As result of the Ce^{3+} ions activity over cathodic IMPs local alkalinisation was lower (pH reached 5.8) compared to reference solution (pH reached 7.5). Thus, Ce^{3+} ions also contributed to inhibit the cathodic activity over the S-phase in this particular case.

According to the modified Pourbaix diagram for the Ce-H$_2$O − HClO$_4$ proposed by Hayes et al. [44], the pH values (~9.1) over graphite in the NaCl reference (non-inhibited) solution [1] were not

high enough to allow formation of stable $Ce(OH)_3$ precipitates (pH = 9.6). However, considering that the SIET probe monitors the pH at approximately 50 μm from the sample surface, these pH values are likely to be underestimated for 0.1-0.6 pH units [45] and, thus, at the surface they might be slightly higher. Moreover, the referred diagram does not take into account the presence of dissolved oxygen in solution, which significantly enlarges the stability zones of Ce(III)/Ce(IV) hydroxides towards lower pH, as proposed elsewhere [44,46]. In other words, the higher the concentration of dissolved O_2, the lower is the pH at which the precipitation of Ce-containing hydroxides (from Ce^{3+} and Ce^{4+}) occurs. In all cases, the pH that allows precipitation of Ce (III/IV) hydroxides certainly was achieved, since yellowish areas (likely to be related with presence of Ce(IV)-containing species [44,47,48]) were clearly observed over graphite after 20 h (Fig. 2(a)).

SEM-EDX analysis carried out on the M1 couple showed that the presence of Ce was assigned to both electrodes (AA2024 and graphite) with the strongest intensity over graphite (Fig. 2(b)). Concerning the alloy regions initially subjected to alkalinisation (Fig. 1(d)), few intermetallic particles were covered by Ce-containing precipitates (Fig. 2(c)), while others seemed protected (Fig. 2 (c, d)). The precipitation of Ce-containing species on AA2024 was expected after the previous electrochemistry study. Importantly, evidences of localised corrosion were not noticed on the alloy surface (Fig. 2(d)) together with vestiges of hydroxychlorides species (pictures not shown). These results suggested that if trenching of the alloy matrix triggered by cathodic particles took place, it was not sufficiently intense to be discriminated during the electrochemical measurements.

Summarizing for the M1couple and for the investigated inhibitor concentration, cerium chloride could control the self-corrosion of AA2024-T3 triggered by local galvanic coupling between matrix and inclusions, but it was not capable of avoiding completely the anodic activity on the alloy induced by coupling with graphite.

3.2. Inhibitive action of cerium on M2

After 1 h of immersion, SVET/SIET monitoring performed on M2 showed a decrease in the cathodic activity around the centre of the graphite (Fig. 3(a)). The corresponding optical micrograph, taken in situ during the measurement, evidenced the formation of a whitish zone (indicated by an arrow in Fig. 3(g)), which can be related to precipitation of cerium containing species. The precipitate was almost colourless (translucent white gel), thus probably containing Ce(III) oxides [44,48]. Previously, in the reference solution [1], there was release of H_2 bubbles (Fig. 3(g)) as result of intense dissolution of the Al matrix followed by acidification due to hydrolysis of Al^{3+} cations (pH = ~4.7, Fig. 3(d)).

During the first SVET/SIET scan, the centre of graphite suffered slight acidification (pH between 5–6, Fig. 3(d)), probably related to diffusion of H^+ from the alloy surface, experiencing intense anodic dissolution, towards regions where generation of OH^- was suppressed due to cerium ions precipitation. Next, as time elapsed, cathodic reactions were progressively supressed on the graphite surface. The maximum cathodic current density decreased from −40 to −30 μA/cm² during the first 2 h and reached −2 μA/cm² after 8 h (Fig. 3(a–c)), respectively). From 8 h up to 20 h, only minor cathodic activities were noticed, being homogeneously distributed over graphite (picture not presented). Concerning the anodic current density related to AA2024, its maximum decreased from 84 to 40 μA/cm² during the first 2 h, attaining 4 μA/cm² after 8 h. This minor anodic activity remained stable until the end of the test.

In the M2 couple, the SIET results were in accordance with the SVET results: from the first scan up to 8 h, alkalinisation related to ORR over graphite was continuously suppressed (pH decreased from 5.7 to 5.4) and the acidification induced by the alloy dissolution was progressively controlled (pH increased slightly from 4.8 to 5.1). After 20 h (picture not presented), the pH values corresponding to the graphite and AA2024 electrodes were respectively around 5.3 and 5.1, while the pH of the bulk electrolyte remained stable at ~5.2.

The results obtained for M2 showed that the cerium-based precipitates offered even higher protection compared to the case of M1, as the magnitude of both maximum anodic and cathodic current densities presented a sharper decrease for longer immersion time. Nonetheless, the minimum pH values over the alloy were systematically lower for M2 (Fig. 4) than for M1 (Fig. 1). The more aggressive conditions, imposed by the higher cathode/anode ratio of M2, force the alloy to display essentially anodic activity. Contrarily, in the M1 couple, AA2024
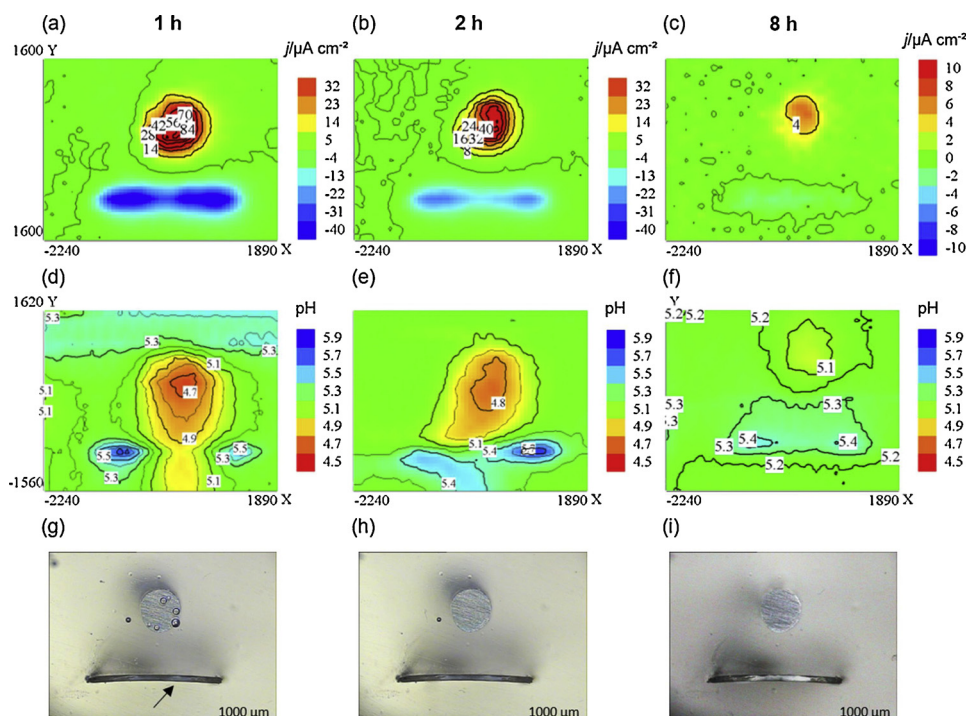

Fig. 3. (a, b, c) Current density (j / μA cm⁻²) and (d, e, f) pH maps obtained for the M2 sample exposed to 8.25 mM NaCl + 1.25 mM $CeCl_3$ after: (a, d) 1 h, (b, e) 2 h and (c, f) 8 h. (g, h, i) corresponding optical micrographs taken in situ after the scans. X and Y coordinates represent the width of the scan in μm.
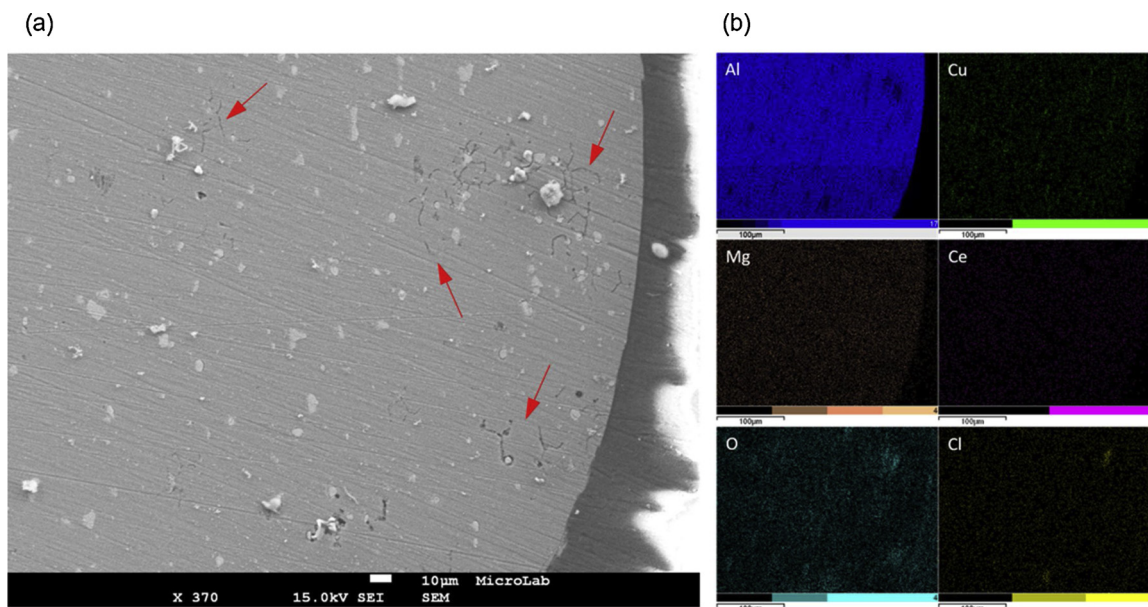
Fig. 4. (a) SEM secondary electron image of the AA2024 surface in the M2 surface after 20 h of exposure to 8.25 mM NaCl + 1.25 mM CeCl$_3$ solution. (b) EDX elemental maps of Al, Cu, Mg, O, Cl and Ce corresponding to the SEM image in (a). The red arrows indicate regions presenting intergranular corrosion. (For interpretation of the references to colour in this figure legend, the reader is referred to the web version of this article).
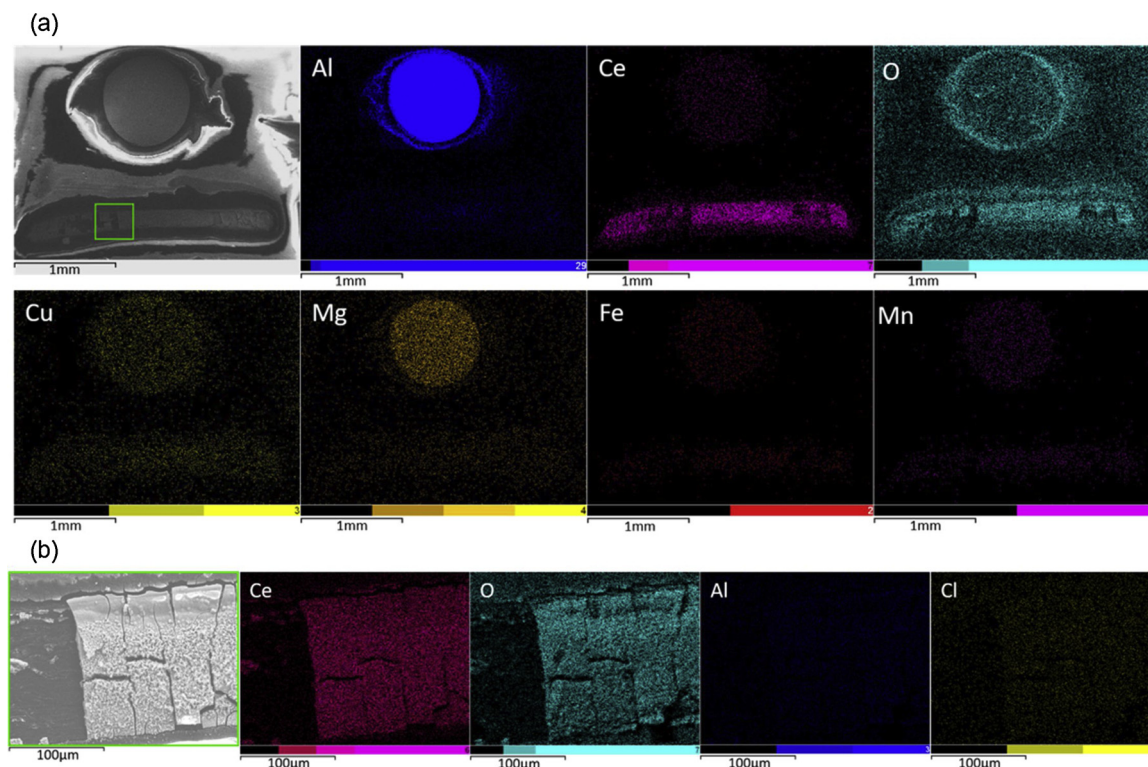

Fig. 5. (a) SEM images on the M2 surface and corresponding EDX elemental maps (Al, Ce, O, Cu, Mg, Fe and Mn) after 20 h of exposure to the 8.25 mM NaCl + 1.25 mM CeCl$_3$ solution. (b) SEM image and EDX elemental maps (Ce, O, Al and Cl) corresponding to the region indicated in (a).

evidenced the presence of both anodic and cathodic regions that could contribute to the underestimation of the acidification (H$^+$ ions could be locally neutralised by the generated alkalinity). The same effect was observed for the M1 couple in the reference electrolyte [1].

SEM-EDX analyses were performed on the M2 sample after 20 h of exposure to the Ce-containing solution. The AA2024 surface appeared protected, although traces of localised corrosion activity, mainly in the form of intergranular corrosion (IGC) were noticed. In Fig. 4(a), the red

arrows indicate regions presenting IGC associated to hydroxychlorides domes (the precipitation of such phases is usual in the reference NaCl medium [1]). Yasakau et al. studied cerium salts [49] and found that such inhibitors are more efficient in preventing pitting corrosion, while they have little influence on limiting corrosion currents, likely related to IGC (obtained at high anodic polarisations).

The alloy precipitates seemed rather intact, as neither trenching nor Mg depletion nor Cu redistribution processes could be detected. Cerium
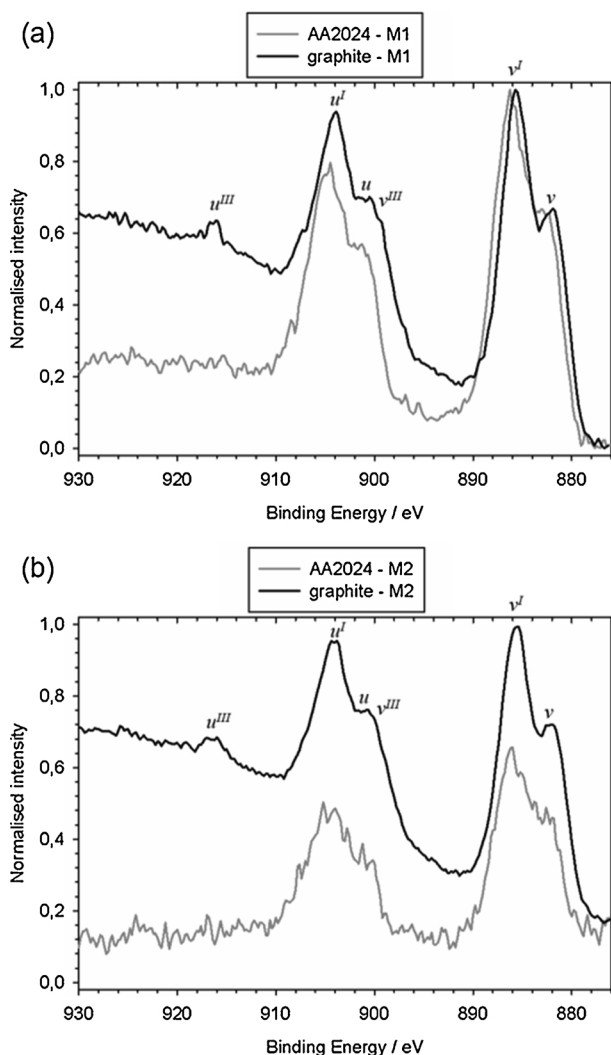
(a)

[Figure: XPS Ce3d photoionization spectra, normalised intensity vs. Binding Energy / eV, legend AA2024 - M1 and graphite - M1]

(b)

[Figure: XPS Ce3d photoionization spectra, normalised intensity vs. Binding Energy / eV, legend AA2024 - M2 and graphite - M2]

Fig. 6. XPS Ce3d photoionization obtained on the AA2024 and graphite surfaces in the samples: (a) M1 and (b) M2 after 20 h of immersion in the 8.25 mM NaCl + 1.25 mM CeCl₃ solution.

species are formed over the alloy, since cerium appeared homogenously distributed on the AA2024 surface (Fig. 4(b)). Contrarily to M1, in which cathodic activity was demonstrated on the AA2024, over M2 the deposition of cerium species suggested that generation of OH^- ions had occurred on the alloy, despite the response provided by SVET-SIET being essentially anodic-related. One possible explanation relies on the fact that local electrochemistry techniques are not always able to resolve ORR related to classical micro-galvanic coupling when it takes place at very low intensities. Alternatively, faster de-alloying of the S-phase could also explain the presence of Ce-containing species on the alloy, as the selective dissolution of Al and Mg would generate OH^- (Eqs. 1 and 2) [49,50]. Thereby, the bubbling verified at the early stages of immersion could be partially related to hydrogen evolution induced by chemical processes. Traces of de-alloying were seldom assigned to AA2024, as S-phase particles were most likely hidden by the precipitation of Ce-containing species.

$$Mg + 2H_2O \rightarrow Mg^{2+} + 2OH^- + H_2\uparrow \qquad (1)$$

$$Mg + 2H_2O \rightarrow Mg^{2+} + 2OH^- + H_2\uparrow \qquad (2)$$
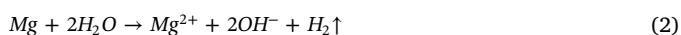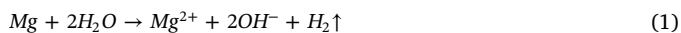
Despite the inhibitive effect of cerium, the distribution of the AA2024 constituent elements (especially Al, Mg and Cu) around the alloy surface (Fig. 5(a)) proved that it was under uniform dissolution. Moreover, its main elements (Al, Cu, Mg, Fe and Mn) could also be

detected at the graphite surface. The metallic cations generated due to the etch out of the matrix were able to meet the alkaline ions generated on the graphite part upon the formation of hydroxide compounds – as predicted for Al^{3+}, Cu^{2+} and Mg^{2+} in the diagram of the activity of species as function of pH [1]. The inset image of the deposits obtained on graphite (Fig. 5(b)) suggested the formation of Al hydroxide/hydroxychlorides besides cerium hydroxides. According to previous work [5], the precipitation of stable $Al(OH)_3$ gel layers on graphite could be responsible for restricting the transport of oxygen to it, also contributing to decrease galvanic activity. Fig. 5(b) also suggested a fragile behaviour of the formed Ce-based species, since several micro-cracks were observed throughout the precipitates. The same fragile morphology was observed for species precipitated on graphite in M1 (pictures not presented). This might have resulted from fast or excessive growth of Ce-containing precipitates [51], induced by the fast kinetics of ORR on graphite. However, dehydration after removing the sample from solution and/or due to the Ultra-High Vacuum conditions of the SEM chamber is likley to induce identical features.

Summarizing, the inhibitive effect of cerium chloride on M2 reduced the extension of the galvanic corrosion between AA2024 and graphite, as observed during SVET/SIET analysis. Eventually, minor local processes responsible for alkalinisation and related to micro-galvanic couplings and/or dealloying of the S-phase were also inhibited. From the SEM-EDX analysis of the post-immersion surfaces, it could be seen that despite limited progression of IGC, a considerable generalised dissolution of the alloy took place.

3.3. XPS analysis after exposure to NaCl/CeCl₃ solution

To determine the valence state of Cerium in the compounds formed on the graphite and alloy surfaces, XPS analyses were performed on M1 and M2 after exposition to 8.25 mM NaCl + 1.25 mM CeCl₃ for 20 h. Fig. 6 (a) and (b) depict the obtained Ce3d photoionization for the samples M1 and M2, respectively. The peaks labelled as v, v^{III} and u, u^{III} refer to $3d_{5/2}$ and $3d_{3/2}$ electron states, respectively and they are indicative for the presence of Ce(IV). The peaks labelled as v^I and u^I refer to $3d_{5/2}$ and $3d_{3/2}$ (respectively) are characteristic of Ce(III) [23]. It had been reported in the literature that the u^{III} peak (mainly detected on the graphite) arose exclusively from Ce^{4+} [52]. But the unresolved peaks in the 895–910 eV range account for the presence of mixture of Ce(IV)/Ce(III) oxidation states [23,44]. Therefore, it can be concluded that the chemical nature of the top surfaces (5–10 nm) from the Ce-based precipitates is essentially the same, regardless the area ratio of the electrodes. Finally, it is important to note that results presented in Fig. 6 are expressed in normalised intensity, but in reality, the Ce concentrations detected were much higher on graphite compared to AA2024: 6.00% vs. 0.82% for M1 and 3.50% vs. 0.16% for M2.

3.4. Effect of triethanolamine addition on M1

As presented in Fig. 7, in the presence of TEA, the corrosion activity in the galvanic couple was reduced; this was well reflected by the progressive suppression of the cathodic activity on graphite. The current densities were considerably lower than those measured in the reference (non-inhibited) electrolyte: after 1 h of exposure to 12.00 mM NaCl, the maximum cathodic and anodic current densities were respectively around -150 and 240 μA/cm², instead of − 20 and 70 μA/cm² in presence of TEA. Despite the inhibiting effect of TEA, few regions on AA2024 remained active, evidencing anodic activity throughout the test (anodic current densities between 40 and 70 μA/cm²).

During the first hour of immersion (Fig. 7(d)), SIET was able to detect a slight pH increase on the alloy surface, contouring the locations of anodic activity that induced local acidification. Since this local pH increase was not coincident with the main cathodic areas, it may be related to chemical dissolution of S-phase [37]. It is worth to note that the pH over anodic zones were much higher (6.0–7.0) than those
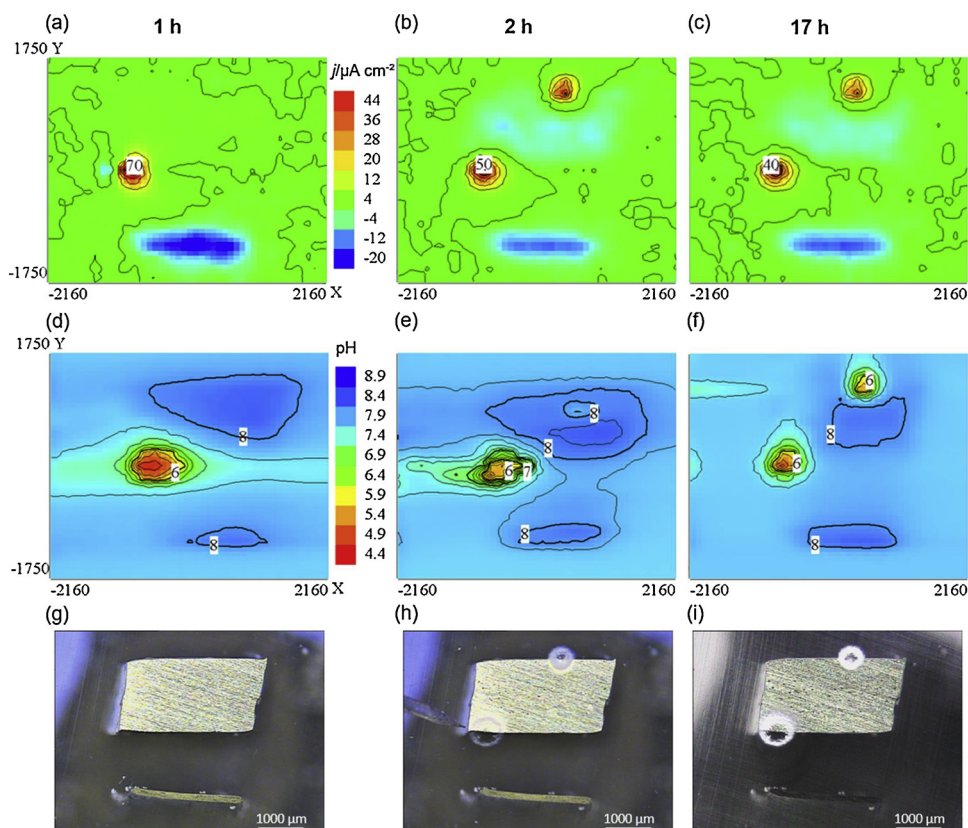
Fig. 7. (a, b, c) Current density (j / µA cm^{-2}) and (d, e, f) pH maps obtained for the M1 sample exposed to the 12.00 mM NaCl + 500 ppm TEA solution after: (a, d) 1 h, (b, e) 2 h and (c) 17 h of exposure. The current density and pH scales are valid for all respective j and pH maps. X and Y coordinates represent the width of the scan in µm.
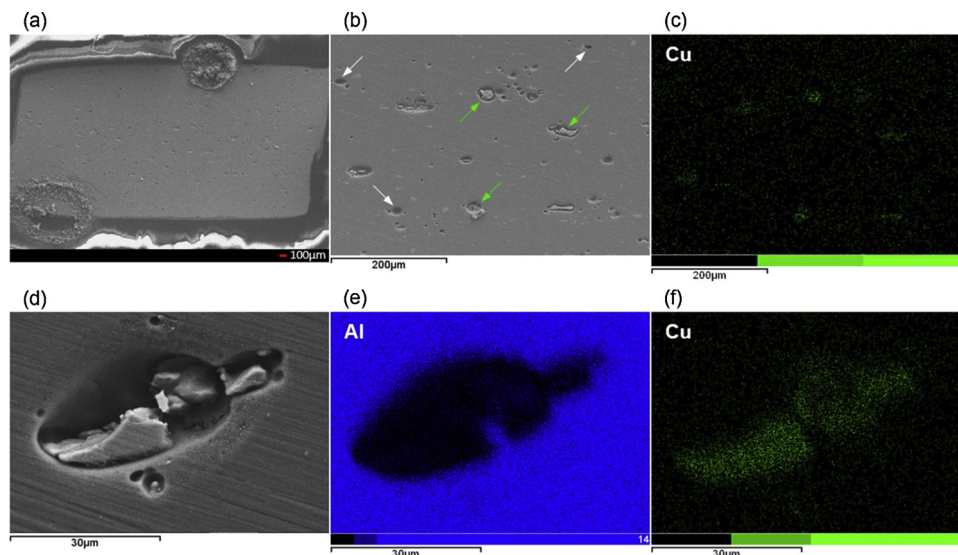

Fig. 8. (a, b, d) SEM images obtained on the AA2024 surface in the M1 sample after 20 h of exposure to the 12.00 mM NaCl + 500 ppm TEA solution. (c) EDX elemental map of Cu corresponding to "(b)". (e, f) EDX mapping of Al and Cu corresponding to "(d)".

measured in the absence of inhibitor (4.5–5.2), most likely, because the presence of TEA initially increased pH of the bulk solution and induced a buffering effect. Starting from 2 h of immersion (Fig. 7(b, e)), cathodic activities were detected over zones of AA2024 highlighting alkalinisation (pH around 8), meaning that ORR extended towards newly formed Cu remnants - just as observed in the reference electrolyte. Until the end of the test, the anodic and cathodic areas (and the corresponding acidification and alkalinisation gradients) remained stable over the alloy.

From the post-immersion SEM-EDX analysis, rings of corrosion products were clearly assigned to the anodic regions on AA2024

(Fig. 8(a)). Considering the pH range recorded above the alloy surface (6.0–8.0), the localised corrosion processes were likely to result from breakdown of the passive layer by Cl$^-$ ions [53]. Furthermore, a trenching process associated to Cu-rich IMPs was clearly evidenced in the regions that presented cathodic activity (Fig. 8 (b, c)). Some part of the produced grooves comprised Cu-rich remnants of modified shape (in comparison to the remnants observed in the reference solution), as indicated by the green arrows, while other small, and round-shaped grooves, were often left completely empty (white arrows). Based on the shape and diameter (around 5 µm), it is plausible to postulate that the Al$_2$CuMg phases were completely dissolved [54–56].
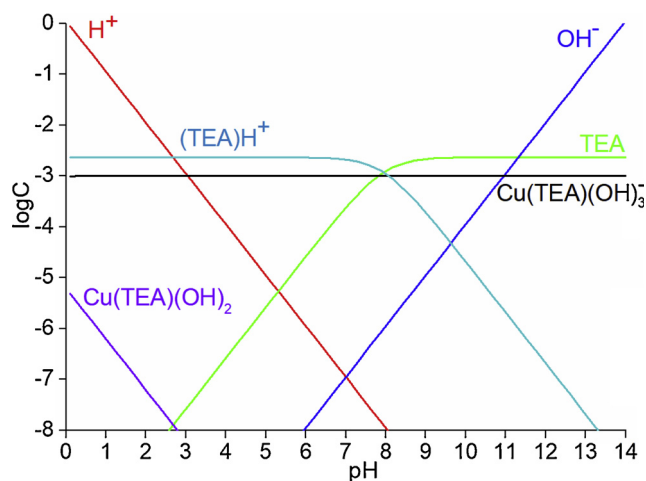
Fig. 9. Logarithm of activity of species in solution as function of pH for Cu^{2+}– TEA complexes. The metal cation and TEA concentrations were 0.1 mM and 3.35 mM, respectively. This diagram was built using the Medusa Software [62] and the stability constants for triethanolamine were taken from Ref. [69].

However, the trenches were different from those that typically occur in the passive layer around IMPs when the AA2024 is immersed in NaCl media and that have been discussed elsewhere [1,57,58]. In Fig. 8(d, e, f), it seems that the Cu-rich particles themselves, rather than the adjacent matrix, were dissolved. Moreover, the trenches observed in the non-inhibited reference solution presented axial growth from the Cu remnants: their propagation could be clearly assigned to dissolution of the alloy matrix. However, in the presence of TEA the grooves evidenced well preserved surfaces, suggesting that their formation was preferentially induced by dissolution of the intermetallic phases.

The Cu remnants observed in (Fig. 8(b, c)) seem to have been originated from relatively large (5–50 μm) and irregular IMPs, probably related to both Al–Cu–Fe–Mn intermetallics and the S-phase [59–61]. According to Ramírez et al. [25], TEA can form coordination compounds with various metals. Therefore, the systematic presence of dissolved Cu-rich remnants might be a consequence of complexation reactions between Cu (and possibly Fe, Mn) and TEA.

Fig. 9 shows a diagram for different species involving the Cu^{2+}-TEA system and it was constructed using the Medusa Software [62] ($[Cu^{2+}] = 0.1$ mM and [TEA] = 3.35 mM). The simulation showed that Cu cations can be complexed by TEA, preferentially forming soluble $Cu(TEA)(OH)_3^-$ species, which are stable regardless the pH. For instance,

TEA might have chelated Cu cations, resulting from Cu enrichment of intermetallics, induced by local alkalinisation. In fact, the trenching processes and S-phase dealloying are known to generate Cu ions (and its eventual re-deposition) [63,64]. Therefore, the formation of the soluble $Cu(TEA)(OH)_3^-$ complexes can explain the strong dissolution of the Cu-rich phases (grooves in Fig. 8) assigned to the cathodic/alkaline regions of AA2024 (Figs. 7).

Cu-rich remnants were not found inside the round-shaped holes assigned to the original Al_2CuMg particles. The large surface of remnants originated from the S-phase self-dissolution [65], often referred as "Swiss cheese" – like morphology, might be the reason for their total consumption: highly exposed Cu-rich surfaces would preferentially react with TEA, increasing the kinetics of $Cu(TEA)(OH)_3^-$ formation. Moreover, this could explain why Cu re-deposition, a process often associated to the S-phase self-dissolution, was not detected (Fig. 8); the Cu ions produced may promptly react with triethanolamine. The prevention of Cu re-deposition around the remnants might also explain the minor propagation of trenches through the Al matrix [66] - in comparison to the trend observed in the reference solution [1].

In conclusion for M1, the inhibitive mechanism of TEA appears to be related to its ability to chelate Cu and other metals (e.g. Fe [67]) present in the alloy IMPs. By decreasing the area of exposed Cu-rich surfaces, TEA decreased the intensity of micro-galvanic couplings between Cu-containing phases and the alloy matrix. Besides, triethanolamine lowered the corrosion intensity on the AA2024/graphite galvanic couple, as the cathodic current density related to graphite considerably declined compared to the reference results.

However, TEA was not sufficiently efficient to protect the alloy from localised anodic dissolution. Protective TEA coordination compounds could not have been indistinctly formed on the entire alloy surface, as they would be rather associated to the Cu-rich intermetallics. At the same time Cu was preferentially removed from the active sites in the form of a soluble complex, leading to formation of empty grooves. As the TEA inhibitive action was considered to proceed via either physical adsorption or chemical coordination [26–28], the limited effect observed on the AA2024/graphite galvanic coupling could be related to the presence of molecules only physically interacting with the alloy passive layer.

3.5. Effect of triethanolamine addition on M2

The galvanic corrosion of M2 appeared to be slightly more controlled with addition of TEA (Fig. 10), compared to the reference solution after 1 h of immersion. However, in case of the inhibitor-
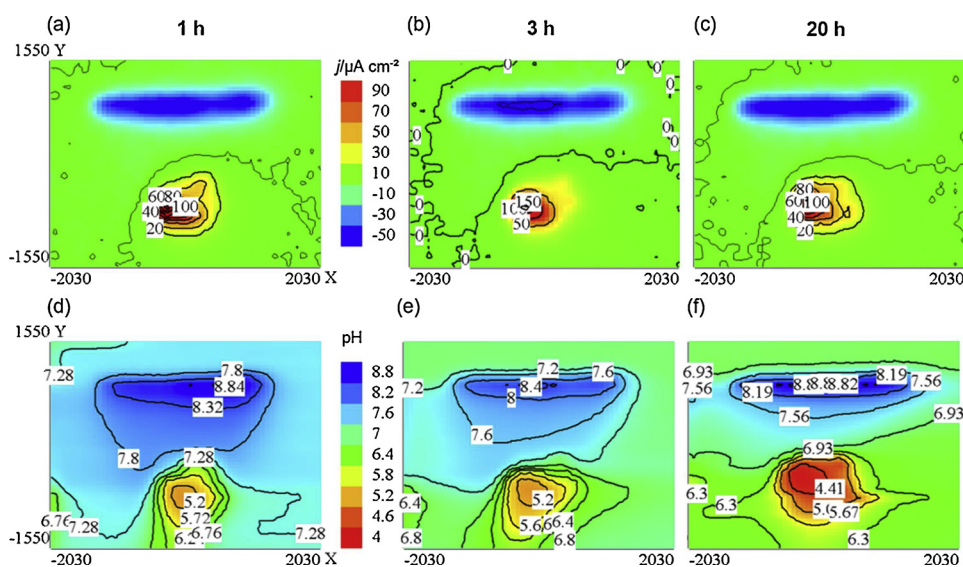

Fig. 10. (a, b, c) Current density (j / μA cm^{-2}) and (d, e, f) pH maps obtained for M2 sample exposed to 12.00 mM NaCl + 500 ppm TEA after: (a, d) 1 h, (b, e) 3 h and (c) 20 h of exposure. The current density and pH scales are valid for all respective j and pH maps. X and Y coordinates represent the width of the scan in μm.
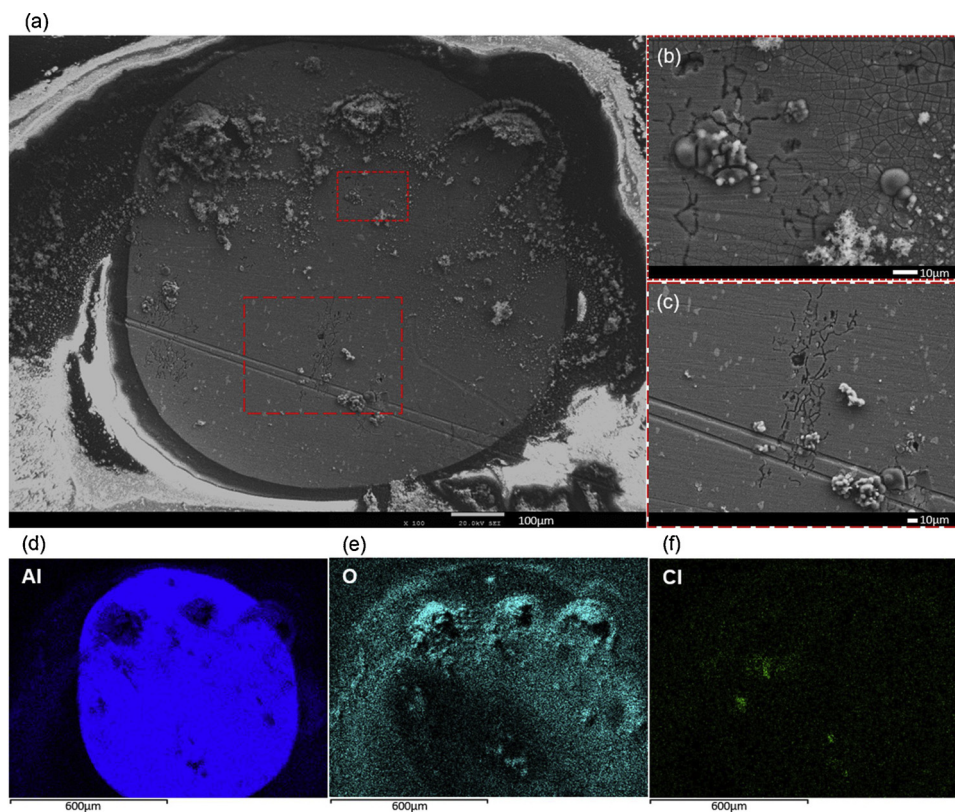
Fig. 11. (a, b, c) SEM images obtained on the AA2024 surface in the M2 sample after 20 h of exposure to 12.00 mM NaCl + 500 ppm TEA solution. "(b)" and "(c)" are insets from "(a)". (d, e, f) corresponding EDX elemental maps (Al, O and Cl) obtained from "(a)".

containing solution, electrochemical activity remained fairly constant up to 20 h, with maximum cathodic and anodic current densities around -50 and 150 μA/cm², respectively. Compared to the behaviour observed in the absence of inhibitor, galvanic activity was progressively suppressed, with anodic and cathodic current densities reaching 34 and −30 μA/cm², respectively, after 20 h of exposure. Therefore, the presence of TEA could not inhibit galvanic corrosion activity even at longer times.

SIET maps showed that the intensity of galvanic corrosion seemed slightly weaker in the presence of TEA. At early immersion stages the pH values measured over graphite and over the alloy surface reached 8.8 and 5.2, respectively, while more extreme values, around 10 and 4.7, respectively, were attained in the reference solution. However, after 20 h, the acidic pH arising from AA2024 reached values around 4.4, which is lower than the values measured in the 12.00 mM NaCl solution (~4.8) – despite the TEA-containing solution being more alkaline (pH = ~7.5) compared to the reference one (pH = ~5.3). Surprisingly, even though more acidic conditions were observed for AA2024 in the presence of TEA, Al hydroxide precipitates were more stable in its presence (Fig. 11(c, d)) than in its absence. Indeed, the structure of the TEA molecule is referred as capable of accelerating the precipitation of hydrated oxides, thus being responsible for favouring the sealing of anodic films on Al [68]. The corrosion products rings that were observed looked similar to those related to the anodic spots of AA2024 in the M1 sample.

Similarly, to the behaviour observed for the M2 sample exposed to 12.00 mM NaCl, the alloy also underwent intergranular corrosion (IGC) besides the generalised dissolution process. Once again, Al hydroxychlorides were detected, and seem associated to regions presenting IGC (Fig. 11 (b) and (c)). The location of the Cl-containing corrosion products corresponded to areas under highest acidification, as monitored by SIET at different immersion times. Although these acidified regions shifted over time, the corresponding previously formed

corrosion products did not dissolve, showing high stability under the conditions of measurement.

SVET/SIET results combined with surface analysis indicated that TEA could not inhibit the corrosion processes observed on AA2024 in the M2 galvanic couple. In the reference solution, despite the intense anodic dissolution of the alloy, the formation of Al hydroxychlorides (yet minor) had limited the extension of galvanic corrosion over time. On the contrary, in the present case, TEA seemed to trigger the precipitation of non-protective corrosion products, by stabilising Al hydroxide phases at lower pH. The compound was not able to chelate Cu from the Al alloy surface, probably due to the limited dissolution of Cu-rich phases in case of M2 sample with higher graphite/AA2024 ratio. This result confirmed that TEA only acted as efficient corrosion inhibitor if the electrochemical conditions for the generation of Cu ions (Cu enrichment processes induced by S-phase de-alloying and/or by trenching phenomena) are created – such as those that occurred on M1 as a result of its less intense galvanic coupling.

4. Conclusions

Quasi-simultaneous SVET/SIET measurements supported by SEM-EDX analysis unveiled the corrosion inhibition mechanisms of cerium chloride and triethanolamine on AA2024-T3/graphite galvanic model couples. The corrosion processes and the corrosion inhibition mechanism of both compounds strongly depend on the ratio of areas between different materials in the couple.

In the couple AA2024/graphite with ratio equal to 10 (M1), cerium chloride effectively inhibited localised corrosion processes on AA2024 and greatly controlled the development of trenching related to Cu-rich precipitates. Similarly, for the lowest AA2024/graphite ratio (M2 = 1.5), the presence of cerium ions limited the extension of intergranular corrosion. However, cerium ions were less effective in inhibiting generalised dissolution of AA2024 induced by coupling with

graphite – which was particularly noticed for M2, due to the increased cathode area. XPS analysis revealed that a mixture of $Ce(OH)_3/Ce(OH)_4$ was present on both AA2024 and graphite surfaces, but at higher concentration over graphite.

Concerning the corrosion inhibition of triethanolamine, the results demonstrated its ability to form complexes with Cu^{2+} ions, under conditions that favour the dissolution of Cu-rich intermetallic particles. However, triethanolamine was shown to be little effective to protect the alloy under anodic dissolution without relevant cathodic activity taking place at the intermetallics. Therefore, the effect provided by triethanolamine on AA2024 was extremely sensitive to the electrodes area ratio: TEA could reduce the extension of trenching of the alloy matrix triggered by Cu-rich IMPs (M1 case), but it was not effective in preventing generalised anodic dissolution and associated intergranular attack in the M2 couple. In fact, for M2, the presence of triethanolamine seemed harmful: the Al hydroxides formed over the acidified regions did not demonstrate protective properties, contrasting to the effect of corrosion products obtained in the NaCl reference solution.

Finally, this investigation stresses the importance of considering different configurations when testing galvanic couples because this helps to select the inhibitors that are likely to be more effective for particular applications.

Data availability

The raw/processed data required to reproduce these findings cannot be shared at this time due to technical or time limitations

Acknowledgements

References

[1] L.B. Coelho, M. Taryba, M. Alves, M.F. Montemor, M. Olivier, Unveiling the effect of the electrodes area on the corrosion mechanism of a graphite – AA2024-T3 galvanic couple by localised electrochemistry, Electrochim. Acta 277 (2018) 9–19, https://doi.org/10.1016/j.electacta.2018.04.187.

[2] F. Bellucci, A. Di Martino, C. Liberti, Electrochemical behaviour of graphite-epoxy composite materials (GECM) in aqueous salt solutions, J. Appl. Electrochem. 16 (1986) 15–22, https://doi.org/10.1007/BF01015979.

[3] S. Payan, Y. Le Petitcorps, J.-M. Olive, H. Saadaoui, Experimental procedure to analyse the corrosion mechanisms at the carbon/aluminium interface in composite materials, Compos. A Appl. Sci. Manuf. 32 (2001) 585–589, https://doi.org/10.1016/S1359-835X(00)00126-3.

[4] M. Serdechnova, S. Kallip, M.G.S. Ferreira, M.L. Zheludkevich, Active self-healing coating for galvanically coupled multi-material assemblies, Electrochem. Commun. 41 (2014) 51–54, https://doi.org/10.1016/j.elecom.2014.01.023.

[5] E. Håkansson, J. Hoffman, P. Predecki, M. Kumosa, The role of corrosion product deposition in galvanic corrosion of aluminum/carbon systems, Corros. Sci. 114 (2017) 10–16, https://doi.org/10.1016/j.corsci.2016.10.011.

[6] R. Srinivasan, L.H. Hihara, Utilization of hydrophobic coatings on insulative skirts to attenuate galvanic corrosion between mechanically-fastened aluminum alloy and carbon-fiber reinforced polymer-matrix composites, Electrochem. Commun. 72 (2016) 96–99, https://doi.org/10.1016/j.elecom.2016.09.014.

[7] P. Visser, H. Terryn, J.M.C. Mol, On the importance of irreversibility of corrosion inhibitors for active coating protection of AA2024-T3, Corros. Sci. 140 (2018) 272–285, https://doi.org/10.1016/j.corsci.2018.05.037.

[8] H. Costenaro, A. Lanzutti, Y. Paint, L. Fedrizzi, M. Terada, H.G. de Melo, M.-G. Olivier, Corrosion resistance of 2524 Al alloy anodized in tartaric-sulphuric acid at different voltages and protected with a TEOS-GPTMS hybrid sol–gel coating, Surf. Coatings Technol. 324 (2017) 438–450, https://doi.org/10.1016/j.surfcoat.2017.05.090.

[9] A. Renaud, M. Poorteman, J. Escobar, L. Dumas, Y. Paint, L. Bonnaud, P. Dubois, M.-G. Olivier, A new corrosion protection approach for aeronautical applications

[10] M. Mohedano, M. Serdechnova, M. Starykevich, S. Karpushenkov, A.C. Bouali, M.G.S. Ferreira, M.L. Zheludkevich, Active protective PEO coatings on AA2024: role of voltage on in-situ LDH growth, Mater. Des. 120 (2017) 36–46, https://doi.org/10.1016/J.MATDES.2017.01.097.

[11] T.T. Thai, M.-E. Druart, Y. Paint, A.T. Trinh, M.-G. Olivier, Influence of the sol–gel mesoporosity on the corrosion protection given by an epoxy primer applied on aluminium alloy 2024–T3, Prog. Org. Coatings. 121 (2018) 53–63, https://doi.org/10.1016/j.porgcoat.2018.04.013.

[12] Y. González-García, J.M.C. Mol, T. Muselle, I. De Graeve, G. Van Assche, G. Scheltjens, B. Van Mele, H. Terryn, A combined mechanical, microscopic and local electrochemical evaluation of self-healing properties of shape-memory polyurethane coatings, Electrochim. Acta 56 (2011) 9619–9626, https://doi.org/10.1016/j.electacta.2011.03.081.

[13] J. Tedim, A.C. Bastos, S. Kallip, M.L. Zheludkevich, M.G.S. Ferreira, Corrosion protection of AA2024-T3 by LDH conversion films, Analysis of SVET results, Electrochim. Acta. 210 (2016) 215–224, https://doi.org/10.1016/j.electacta.2016.05.134.

[14] D. Snihirova, S.V. Lamaka, P. Taheri, J.M.C. Mol, M.F. Montemor, Comparison of the synergistic effects of inhibitor mixtures tailored for enhanced corrosion protection of bare and coated AA2024-T3, Surf. Coat. Technol. 303 (2016) 342–351, https://doi.org/10.1016/j.surfcoat.2015.10.075.

[15] S.A.S. Dias, S.V. Lamaka, C.A. Nogueira, T.C. Diamantino, M.G.S. Ferreira, Sol–gel coatings modified with zeolite fillers for active corrosion protection of AA2024, Corros. Sci. 62 (2012) 153–162, https://doi.org/10.1016/j.corsci.2012.05.009.

[16] P.J. Denissen, S.J. Garcia, Cerium-loaded algae exoskeletons for active corrosion protection of coated AA2024-T3, Corros. Sci. 128 (2017) 164–175, https://doi.org/10.1016/j.corsci.2017.09.019.

[17] T.L.P. Galvão, I. Sousa, M. Wilhelm, J. Carneiro, J. Opršal, H. Kukačková, V. Špaček, F. Maia, J.R.B. Gomes, J. Tedim, M.G.S. Ferreira, Improving the functionality and performance of AA2024 corrosion sensing coatings with nanocontainers, Chem. Eng. J. 341 (2018) 526–538, https://doi.org/10.1016/j.cej.2018.02.061.

[18] M. Abdolah Zadeh, J. Tedim, M. Zheludkevich, S. van der Zwaag, S.J. Garcia, Synergetic active corrosion protection of AA2024-T3 by 2D- anionic and 3D-cationic nanocontainers loaded with Ce and mercaptobenzothiazole, Corros. Sci. 135 (2018) 35–45, https://doi.org/10.1016/j.corsci.2018.02.018.

[19] J.S. Laird, A.E. Hughes, C.G. Ryan, P. Visser, H. Terryn, J.M.C. Mol, Particle induced gamma and X-ray emission spectroscopies of lithium based alloy coatings, Nucl. Instruments Methods Phys. Res. Sect. B Beam Interact. Mater. Atoms 404 (2017) 167–172, https://doi.org/10.1016/j.nimb.2017.03.088.

[20] L.B. Coelho, M.-G. Olivier, The inhibition efficiency of different species on AA2024/graphite galvanic coupling models depicted by SVET, Corros. Sci. 136 (2018) 292–303, https://doi.org/10.1016/j.corsci.2018.03.015.

[21] B.R.W. Hinton, D.R. Arnott, N.E. Ryan, The inhibition of aluminium alloy corrosion by cerous cations, Met. Forum. 7 (4) (1984) 211–217.

[22] B.R.W. Hinton, D.R. Arnott, N.E. Ryan, Cerium conversion coatings for the corrosion protection of Aluminium, Met. Forum. 9 (1986) 162–173.

[23] E.A. Matter, S. Kozhukharov, M. Machkova, V. Kozhukharov, Comparison between the inhibition efficiencies of Ce(III) and Ce(IV) ammonium nitrates against corrosion of AA2024 aluminum alloy in solutions of low chloride concentration, Corros. Sci. 62 (2012) 22–33, https://doi.org/10.1016/j.corsci.2012.03.039.

[24] P. Rodič, I. Milošev, Corrosion inhibition of pure aluminium and alloys AA2024-T3 and AA7075-T6 by cerium(III) and cerium(IV) salts, J. Electrochem. Soc. 163 (2016) C85–C93, https://doi.org/10.1149/2.0431603jes.

[25] C. Ramírez, J.A. Calderón, Study of the effect of triethanolamine as a chelating agent in the simultaneous electrodeposition of copper and zinc from non-cyanide electrolytes, J. Electroanal. Chem. 765 (2016) 132–139, https://doi.org/10.1016/j.jelechem.2015.06.003.

[26] H. Choi, Y.K. Song, K.Y. Kim, J.M. Park, Encapsulation of triethanolamine as organic corrosion inhibitor into nanoparticles and its active corrosion protection for steel sheets, Surf. Coat. Technol. 206 (2012) 2354–2362, https://doi.org/10.1016/j.surfcoat.2011.10.030.

[27] W. Shang, C. He, Y. Wen, Y. Wang, Z. Zhang, Performance evaluation of triethanolamine as corrosion inhibitor for magnesium alloy in 3.5 wt% NaCl solution, RSC Adv. 6 (2016) 113967–113980, https://doi.org/10.1039/C6RA23203E.

[28] H. Bi, G.T. Burstein, B.B. Rodriguez, G. Kawaley, Some aspects of the role of inhibitors in the corrosion of copper in tap water as observed by cyclic voltammetry, Corros. Sci. 102 (2016) 510–516, https://doi.org/10.1016/j.corsci.2015.11.005.

[29] M. Zhang, Yi Long, Inhibition of triethanolamine for magnetic refrigeration material LaFe11.0Co0.7Si1.3 in distilled Water, Proc. 7th Natl. Conf. Funct. Mater. Appl. (2010), pp. 1706–1707 http://file.scirp.org/pdf/22-1.396.pdf.

[30] A.-M.-C. Dumitriu, M. Cazacu, A. Bargan, S. Shova, C. Turta, Cu(II) and Ni(II) complexes with a tri-, tetra- or hexadentate triethanolamine ligand: Structural characterization and properties, Polyhedron 50 (2013) 255–263, https://doi.org/10.1016/j.poly.2012.11.009.

[31] B.R. Horrocks, M.V. Mirkin, D.T. Pierce, A.J. Bard, G. Nagy, K. Toth, Scanning electrochemical microscopy. 19. Ion-selective potentiometric microscopy, Anal. Chem. 65 (1993) 1213–1224, https://doi.org/10.1021/ac00057a019.

[32] C. Wei, A.J. Bard, G. Nagy, K. Toth, Scanning electrochemical microscopy. 28. Ion-selective neutral carrier-based microelectrode potentiometry, Anal. Chem. 67 (1995) 1346–1356, https://doi.org/10.1021/ac00104a008.

[33] S.V. Lamaka, O.V. Karavai, A.C. Bastos, M.L. Zheludkevich, M.G.S. Ferreira, Monitoring local spatial distribution of Mg2+, pH and ionic currents, Electrochem.

Commun. 10 (2008) 259–262, https://doi.org/10.1016/J.ELECOM.2007.12.003.

[34] S.V. Lamaka, M. Taryba, M.F. Montemor, H.S. Isaacs, M.G.S. Ferreira, Quasi-simultaneous measurements of ionic currents by vibrating probe and pH distribution by ion-selective microelectrode, Electrochem. Commun. 13 (2011) 20–23, https://doi.org/10.1016/j.elecom.2010.11.002.

[35] M. Taryba, S.V. Lamaka, D. Snihirova, M.G.S. Ferreira, M.F. Montemor, W.K. Wijting, S. Toews, G. Grundmeier, The combined use of scanning vibrating electrode technique and micro-potentiometry to assess the self-repair processes in defects on "smart" coatings applied to galvanized steel, Electrochim. Acta 56 (2011) 4475–4488, https://doi.org/10.1016/j.electacta.2011.02.048.

[36] A. Alvarez-Pampliega, S.V. Lamaka, M.G. Taryba, M. Madani, J. De Strycker, E. Tourwé, M.G.S. Ferreira, H. Terryn, Cut-edge corrosion study on painted aluminum rich metallic coated steel by scanning vibrating electrode and micro-potentiometric techniques, Electrochim. Acta 61 (2012) 107–117, https://doi.org/10.1016/j.electacta.2011.11.110.

[37] H. Shi, Z. Tian, T. Hu, F. Liu, E.H. Han, M. Taryba, S.V. Lamaka, Simulating corrosion of Al_2CuMg phase by measuring ionic currents, chloride concentration and pH, Corros. Sci. 88 (2014) 178–186, https://doi.org/10.1016/j.corsci.2014.07.021.

[38] M.G. Taryba, M.F. Montemor, S.V. Lamaka, Quasi-simultaneous mapping of local current density, pH and dissolved O_2, Electroanalysis 27 (2015) 2725–2730, https://doi.org/10.1002/elan.201500286.

[39] H. Shi, E.-H. Han, F. Liu, T. Wei, Z. Zhu, D. Xu, Study of corrosion inhibition of coupled Al_2Cu–Al and Al_3Fe–Al by cerium cinnamate using scanning vibrating electrode technique and scanning ion-selective electrode technique, Corros. Sci. 98 (2015) 150–162, https://doi.org/10.1016/j.corsci.2015.05.019.

[40] S. Wang, H. Ming, J. Ding, Z. Zhang, J. Wang, E.H. Han, A. Atrens, Effect of H3BO3 on corrosion in 0.01 M NaCl solution of the interface between low alloy steel A508 and alloy 52 M, Corros. Sci. 102 (2016) 469–483, https://doi.org/10.1016/j.corsci.2015.10.040.

[41] D. Snihirova, M. Taryba, S.V. Lamaka, M.F. Montemor, Corrosion inhibition synergies on a model Al–Cu–Mg sample studied by localized scanning electrochemical techniques, Corros. Sci. 112 (2016) 408–417, https://doi.org/10.1016/j.corsci.2016.08.040.

[42] E.A. Zdrachek, A.G. Karotkaya, V.A. Nazarov, K.A. Andronchyk, L.S. Stanishevskii, V.V. Egorov, M.G. Taryba, D. Snihirova, M. Kopylovich, S.V. Lamaka, H + -selective microelectrodes with optimized measuring range for corrosion studies, Sens. Actuators B Chem. 207 (2015) 967–975, https://doi.org/10.1016/j.snb.2014.07.106.

[43] D.A. Shirley, High-resolution X-ray photoemission spectrum of the valence bands of gold, Phys. Rev. B 5 (1972) 4709–4714, https://doi.org/10.1103/PhysRevB.5.4709.

[44] S.A. Hayes, P. Yu, T.J. O'Keefe, M.J. O'Keefe, J.O. Stoffer, The phase stability of cerium species in aqueous systems, J. Electrochem. Soc. 149 (2002) C623, https://doi.org/10.1149/1.1516775.

[45] O. Dolgikh, A. Demeter, S.V. Lamaka, M. Taryba, A.C. Bastos, M.C. Quevedo, J. Deconinck, Simulation of the role of vibration on scanning vibrating electrode technique measurements close to a disc in plane, Electrochim. Acta 203 (2016) 379–387, https://doi.org/10.1016/j.electacta.2016.01.188.

[46] P. Yu, S.A. Hayes, T.J. O'Keefe, M.J. O'Keefe, J.O. Stoffer, The phase stability of cerium species in aqueous systems, J. Electrochem. Soc. 153 (2006) C74, https://doi.org/10.1149/1.2130572.

[47] B. Davó, A. Conde, J.J. De Damborenea, Inhibition of stress corrosion cracking of alloy AA8090 T-8171 by addition of rare earth salts, Corros. Sci. 47 (2005) 1227–1237, https://doi.org/10.1016/j.corsci.2004.07.028.

[48] A.J. Davenport, H.S. Isaacs, M.W. Kendig, XANES investigation of the role of cerium compounds as corrosion inhibitors for aluminum, Corros. Sci. 32 (1991) 653–663, https://doi.org/10.1016/0010-938X(91)90113-4.

[49] K.A. Yasakau, M.L. Zheludkevich, S.V. Lamaka, M.G.S. Ferreira, Mechanism of corrosion inhibition of AA2024 by rare-earth compounds, J. Phys. Chem. B 110 (2006) 5515–5528, https://doi.org/10.1021/jp0560664.

[50] L. Paussa, F. Andreatta, D. De Felicis, E. Bemporad, L. Fedrizzi, Investigation of AA2024-T3 surfaces modified by cerium compounds: a localized approach, Corros. Sci. 78 (2014) 215–222, https://doi.org/10.1016/j.corsci.2013.10.001.

[51] L.B. Coelho, D. Cossement, M.-G. Olivier, Benzotriazole and cerium chloride as corrosion inhibitors for AA2024-T3: an EIS investigation supported by SVET and ToF-SIMS analysis, Corros. Sci. 130 (2018) 177–189, https://doi.org/10.1016/j.corsci.2017.11.004.

[52] X. Yu, G. Li, XPS study of cerium conversion coating on the anodized 2024 aluminum alloy, J. Alloys. Compd. 364 (2004) 193–198, https://doi.org/10.1016/S0925-8388(03)00502-4.

[53] G.S. Chen, M. Gao, R.P. Wei, Microconstituent-induced pitting corrosion in aluminum alloy 2024-T3, Corrosion 52 (1996) 8–15, https://doi.org/10.5006/1.3292099.

[54] R.G. Buchheit, Local dissolution phenomena associated with S phase (Al2CuMg) particles in aluminum alloy 2024-T3, J. Electrochem. Soc. 144 (1997) 2621, https://doi.org/10.1149/1.1837874.

[55] L. Lacroix, L. Ressier, C. Blanc, G. Mankowski, Combination of AFM, SKPFM, and SIMS to study the corrosion behavior of S-phase particles in AA2024-T351, J. Electrochem. Soc. 155 (2008) C131–C137, https://doi.org/10.1149/1.2833315.

[56] A. Boag, R.J. Taylor, T.H. Muster, N. Goodman, D. McCulloch, C. Ryan, B. Rout, D. Jamieson, A.E. Hughes, Stable pit formation on AA2024-T3 in a NaCl environment, Corros. Sci. 52 (2010) 90–103, https://doi.org/10.1016/j.corsci.2009.08.043.

[57] A. Boag, A.E. Hughes, A.M. Glenn, T.H. Muster, D. McCulloch, Corrosion of AA2024-T3 part I: localised corrosion of isolated IM particles, Corros. Sci. 53 (2011) 17–26, https://doi.org/10.1016/j.corsci.2010.09.009.

[58] J.A. Moreto, C.E.B. Marino, W.W. Bose Filho, L.A. Rocha, J.C.S. Fernandes, SVET, SKP and EIS study of the corrosion behaviour of high strength Al and Al–Li alloys used in aircraft fabrication, Corros. Sci. 84 (2014) 30–41, https://doi.org/10.1016/j.corsci.2014.03.001.

[59] M.A. Jakab, D.A. Little, J.R. Scully, Experimental and modeling studies of the oxygen reduction reaction on AA2024-T3, J. Electrochem. Soc. (2005) 311–320, https://doi.org/10.1149/1.1949047.

[60] L. Lacroix, L. Ressier, C. Blanc, G. Mankowski, Statistical study of the corrosion behavior of Al2CuMg intermetallics in AA2024-T351 by SKPFM, J. Electrochem. Soc. 155 (2008) C8, https://doi.org/10.1149/1.2799089.

[61] W. Qafsaoui, M.W. Kendig, H. Perrot, H. Takenouti, Effect of 1-pyrrolidine dithio-carbamate on the galvanic coupling resistance of intermetallics – aluminum matrix during corrosion of AA 2024-T3 in a dilute NaCl, Corros. Sci. 92 (2015) 245–255, https://doi.org/10.1016/j.corsci.2014.12.011.

[62] I. Puigdomenech, Program MEDUSA (Make Equilibrium Diagrams Using Sophisticated Algorithms), (2016) https://sites.google.com/site/chemdiagr/.

[63] A.E. Hughes, R. Parvizi, M. Forsyth, Microstructure and corrosion of AA2024, Corros. Rev. 33 (2015) 1–30, https://doi.org/10.1515/corrrev-2014-0039.

[64] C. Laurent, F. Scenini, T. Monetta, F. Bellucci, M. Curioni, The contribution of hydrogen evolution processes during corrosion of aluminium and aluminium alloys investigated by potentiodynamic polarisation coupled with real-time hydrogen measurement, Npj Mater. Degrad. 1 (2017) 6, https://doi.org/10.1038/s41529-017-0011-4.

[65] N. Dimitrov, J.A. Mann, M. Vukmirovic, K. Sieradzki, Dealloying of Al[sub 2]CuMg in alkaline media, J. Electrochem. Soc. 147 (2000) 3283–3285, https://doi.org/10.1149/1.1393896.

[66] T. Suter, R.C. Alkire, microelectrochemical studies of pit initiation at single inclusions in Al 2024-T3, J. Electrochem. Soc. 148 (2001) B36, https://doi.org/10.1149/1.1344530.

[67] C. Goujon, T. Pauporté, C. Mansour, S. Delaunay, J.-L. Bretelle, Electrochemical deposition of thick iron oxide films on nickel based superalloy substrates, Electrochim. Acta 176 (2015) 230–239, https://doi.org/10.1016/j.electacta.2015.06.045.

[68] A. Bautista, J.A. González, V. López, Influence of triethanolamine additions on the sealing mechanism of anodised aluminium, Surf. Coat. Technol. 154 (2002) 49–54, https://doi.org/10.1016/S0257-8972(01)01667-X.

[69] P. De Vreese, A. Skoczylas, E. Matthijs, J. Fransaer, K. Binnemans, Electrodeposition of copper–zinc alloys from an ionic liquid-like choline acetate electrolyte, Electrochim. Acta 108 (2013) 788–794, https://doi.org/10.1016/j.electacta.2013.06.140.